Understanding the Saturation Power of Josephson Parametric Amplifiers Made from SQUID Arrays

Luca Planat,[1] Rémy Dassonneville,[1] Javier Puertas Martínez,[1] Farshad Foroughi,[1] Olivier Buisson,[1] Wiebke Hasch-Guichard,[1] Cécile Naud,[1] R. Vijay,[2] Kater Murch,[3] and Nicolas Roch[1,*]

[1] *Université Grenoble Alpes, CNRS, Grenoble INP, Institut Néel, 38000 Grenoble, France*

[2] *Tata Institute of Fundamental Research, Mumbai, India*

[3] *Washington University in St. Louis, St. Louis, Missouri, USA*

(Received 21 September 2018; revised manuscript received 17 December 2018; published 6 March 2019)

We report on the implementation and detailed modeling of a Josephson parametric amplifier (JPA) made from an array of eighty superconducting quantum interference devices (SQUIDs), forming a nonlinear quarter-wave resonator. This device is fabricated using a very simple single-step fabrication process. It shows a large bandwidth (45 MHz), an operating frequency tunable between 5.9 and 6.8 GHz, and a large input saturation power (−117 dBm) when biased to obtain 20 dB of gain. Despite the length of the SQUID array being comparable to the wavelength, we present a model based on an effective nonlinear *LC* series resonator that quantitatively describes these figures of merit without fitting parameters. Our work illustrates the advantage of using array-based JPA since a single-SQUID device showing the same bandwidth and resonant frequency would display a saturation power 15 dB lower.

DOI: 10.1103/PhysRevApplied.11.034014

I. INTRODUCTION

Gain, bandwidth, and noise performance ultimately dictate the quantum efficiency and speed of quantum measurements performed at microwave frequencies in the circuit quantum electrodynamics architecture. Improving these three properties of an amplifier has been the driving force for Josephson-junction-based amplifier design and characterization, including significant work optimizing bandwidth [1,2], pump rejection using flux or nondegenerate pumping schemes [3–8], and realizing directionality in the amplification process [9–11]. Josephson-junction-based parametric amplifiers utilize the intrinsic nonlinearity of the junction as the basis for parametric wave mixing. Controlling the type and strength of this nonlinearity has been the focus of several amplifier designs since this quantity imposes the input saturation power (characterized as the 1-dB compression point) of such amplifiers [12–18]. Moreover, when the strength of the nonlinearity reaches a few percent of the operating frequency of the device, higher-order effects lead to imperfect squeezing and nonquantum-limited performance [19–21]. However, it is only very recently that the fourth-order nonlinearity or Kerr nonlinearity was identified as the main cause of Josephson parametric amplifier saturation [17]. In their work, Liu *et al.* did not manage to relate the effective nonlinearity of their Josephson junction amplifier to the actual circuit model. This outstanding goal was achieved soon after in the case of the SNAIL parametric amplifier, a Josephson device operated in a three-wave mixing mode [18]. In this article, we present a parametric amplifier based on four-wave mixing. The subtlety here is that the nonlinearity at the root of parametric amplification is the same as the one causing saturation. Our device is formed by a high-impedance Josephson metamaterial—an array of $N = 80$ SQUIDs—that forms a $\lambda/4$ nonlinear resonator [22–25]. The dispersion relation of this SQUIDs array, obtained via two-tone spectroscopy, is fitted using a long-range Coulomb interaction or "remote ground" model [26], leading to independently inferred values of the circuit components (capacitances and SQUIDs' critical current). We show that the amplifier can be quantitatively described by an effective nonlinear *LC* series resonator with a resonant frequency near the first resonant mode of the array. We report a good quantitative agreement between the saturation power of this Josephson parametric amplifier (JPA) and a model without fitting parameters. According to this theory, the 80-SQUID array yields a 15-dB improvement over a comparable single SQUID device.

This article is organized as follows. In Sec. II, we present an effective model and review the basic description of our device as a single-port degenerate Josephson parametric amplifier and, in Sec. III, we discuss how arrays of SQUIDs can effectively reduce the nonlinearity of the device, leading to increased saturation power. In Sec. IV, we present the device and Sec. V describes its properties

*nicolas.roch@neel.cnrs.fr

in the linear regime. Gain and saturation are reported in Sec. VI, while we discuss the main results in Sec. VII.

II. MODEL

Our device (see Fig. 1) can be modeled as an effective single-port, degenerate Josephson parametric amplifier employing a nonlinearity of the Kerr type. The circuit can be described by the Hamiltonian of a nonlinear resonator:

$$H_{\mathrm{JPA}} = \hbar\omega_{\mathrm{eff}} A^\dagger A + \hbar\frac{K_{\mathrm{eff}}}{2}\left(A^\dagger\right)^2 A^2, \tag{1}$$

where A is the annihilation operator of the intraresonator field. It is characterized by an effective resonant frequency ω_{eff}, a nonlinearity or self-Kerr coefficient K_{eff}, and a coupling rate to a transmission line κ_{eff}. The link between the circuit model and these effective parameters is explained in Sec. V. The JPA is powered by a monochromatic current pump. The physics of such degenerate Josephson parametric amplifiers has been explained in great detail in various articles [2,19,21,27]. We recall here the main equations, following the approach of Eichler and Wallraff [14]. The dynamics of the circuit is inferred using conventional input-output theory:

$$\dot{A} = -i\omega_{\mathrm{eff}} A - iK_{\mathrm{eff}} A^\dagger AA - \frac{\kappa_{\mathrm{eff}}}{2}A + \sqrt{\kappa_{\mathrm{eff}}}A_{\mathrm{in}}, \tag{2}$$

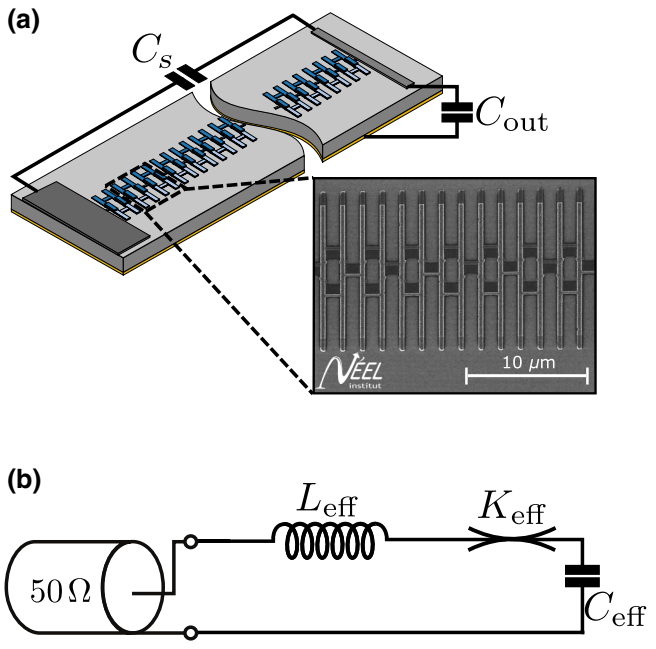

FIG. 1. (a) Sketch of the JPA based on an array of 80 SQUIDs. We highlight the capacitance C_{out} between the last superconducting pad and the ground and the parasitic shunt capacitance C_s between the input/output pad and the last superconducting pad. Enlargement: SEM image of seven identical SQUIDs, where a single junction has an area of 10.7×0.370 μm. (b) Effective LC series nonlinear resonator.

with A_{in} the input field coupled with rate κ_{eff}. The boundary conditions of the resonator are taken into account via the equation $A_{\mathrm{out}} = \sqrt{\kappa_{\mathrm{eff}}}A - A_{\mathrm{in}}$, where A_{out} is the output field. Next, we assume that $A = \alpha + \hat{a}$, where α is a classical part (referring to the strong coherent pump) and $\hat{a}$ is the signal that we treat quantum mechanically. To obtain the gain of the amplifier we follow a two-step procedure: we first solve for the classical field α while setting $\langle\hat{a}\rangle = 0$ and then we use a linearization of the equation of motion for $\hat{a}$ around this working point (see Appendix E for a detailed derivation). This leads to the standard equation of a parametric amplifier:

$$\hat{a}_{\mathrm{out}}(\Delta) = g_{S,\Delta}\hat{a}_{\mathrm{in}}(\Delta) + g_{I,\Delta}\hat{a}^\dagger_{\mathrm{in}}(-\Delta). \tag{3}$$

The operators $\hat{a}_{\mathrm{in}}(\Delta)$ and $\hat{a}_{\mathrm{out}}(\Delta)$ are the Fourier components of the input and outputs signals, where Δ is the dimensionless frequency detuning $\Delta = (\omega_p - \omega_{\mathrm{signal}})/\kappa$ from the pump frequency. Equation (3) illustrates the link between the output signal and the inputs at signal (Δ) and idler ($-\Delta$) frequencies. Signal and idler gain ($g_{S,\Delta}$ and $g_{I,\Delta}$, respectively) are expressed as

$$g_{S,\Delta} = -1 + \frac{i(\delta - 2\xi_\alpha n - \Delta) + \frac{1}{2}}{(i\Delta - \lambda_-)(i\Delta - \lambda_+)} \tag{4a}$$

$$g_{I,\Delta} = \frac{-i\xi_\alpha n e^{2i\phi}}{(i\Delta - \lambda_-)(i\Delta - \lambda_+)}, \tag{4b}$$

with $\lambda_\pm = \frac{1}{2} \pm \sqrt{((\xi_\alpha n)^2 - (\delta - 2\xi_\alpha n))}$ (a complete derivation is given in Appendix E). Both of them encompass the dimensionless detuning δ between the pump and bare resonator frequencies, ξ_α the product between the nonlinearity and the pump power, n the normalized number of pump photons in the cavity, ϕ the phase difference between the pump and the signal, and Δ. The exact expressions for these parameters are given in Appendix E. $|g_{S,\Delta}|^2$ is plotted in Fig. 2, using the parameters of our amplifier, as a function of the pump power and pump frequency for zero detuning between the pump and the signal ($\Delta = 0$). We define the optimal pump frequency $f_{p,\mathrm{opt}}$ as the one which maximizes the gain for a given pump power, as shown in Eq. (4). $\Delta f_p = f_p - f_{p,\mathrm{opt}}$ is a frequency shift from optimal pumping conditions. As illustrated in the inset of Fig. 2, Δf_p as small as 5 MHz leads to a reduction of the gain in excess of 1 dB. This observation is at the heart of JPA saturation [17], since an input power of n_s signal photons per second leads to a shift $\Delta f_p \approx n_s \times K_{\mathrm{eff}}/\kappa_{\mathrm{eff}}$ Hertz from optimal pumping frequency, thus leading to a drop of the maximum expected gain. This qualitative explanation will be further formalized in Sec. VI and it can be shown that the input saturation power of JPA increases linearly with the ratio $\kappa_{\mathrm{eff}}/|K_{\mathrm{eff}}|$ [14]. Maximizing this ratio, and thus minimizing the nonlinear self-Kerr term K_{eff}, is therefore of prime importance.

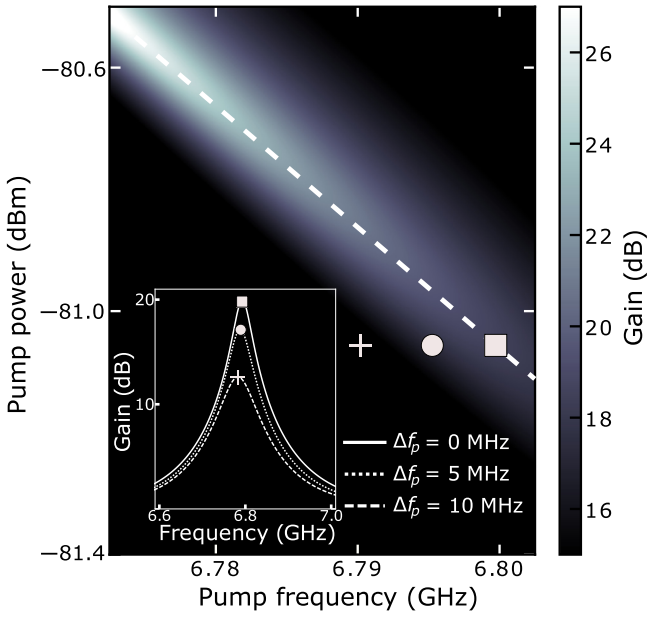

FIG. 2. Theoretical maximum signal gain $|g_{S,\Delta}|^2$ versus pump power and pump frequency for signal detuning $\Delta = 0$. Larger gain requires larger pump power and lower pump frequency. The inset shows the gain versus frequency for three different pump configurations as indicated by the markers. The maximum expected gain for a given pump power (white square) is reduced when the pump frequency is slightly detuned from this optimal point (circle and cross).

III. DECREASING NONLINEARITY USING ARRAYS

Because reduced K_{eff} is important to improve dynamical range, several methods have been introduced to reduce nonlinearity in parametric amplifiers. One first option is to use the intrinsic nonlinearity of superconductors such as niobium [28], NbN [29], or granular aluminum [30], since they often come with very weak nonlinearities spanning from 20 mHz to 30 kHz for resonators in the GHz range. However, these nonlinearities are so weak that extremely large pump powers are required, resulting in experimental challenges. Another option is to dilute the nonlinearity of a single Josephson junction into a larger and linear resonator [15,31]. However, in this case, the Josephson junction is not purely phase-biased anymore and the usual quartic approximation used to treat the Josephson potential has a limited validity [14,21]. Already in the early days of Josephson parametric amplifiers, it was recognized that using an array of N Josephson junctions could be beneficial [22]. In this case, the total phase drop Φ_{tot} (or equivalently the voltage drop) occurs across the whole array and not across a single junction. Thus, the nonlinearity is divided by N since each junction experiences a phase drop Φ_{tot}/N (see Appendix B for a derivation). This idea can be pushed further by fabricating an array of N Josephson junctions with a critical current N times larger; the nonlinearity is then divided by N^2 [14,15,32]. However, the approximation that each junction experiences a Φ_{tot}/N phase drop loses validity when the system becomes very large, reaching a size comparable to the wavelength of the microwave signal. In this case, propagating effects should be accounted for properly.

To do so, we start by defining the normal modes of the circuit and then treat the nonlinearity perturbatively as described in previous works [33–35]. Each SQUID is considered as an LC parallel oscillator, described by C_J and L_J. However, describing the chain as a standard transmission line as it is routinely done, where every LC oscillator is shunted to the ground via a ground capacitance C_g, is not the most appropriate description for our system. Given that the distance between the chain and the ground plane is comparable or greater than the modes wavelength [see Fig. 1(a)], the screening of the charges by the ground plane cannot be considered as local. Capacitive effects between SQUIDs must be accounted for via the long-range part of the Coulomb interaction. We follow the procedure described by Krupko *et al.* [26] to take this long-range interaction into consideration. This remote ground model gives results closer to the experiment than the standard transmission line model (see Appendix D). Although this remote ground model is more complex than the standard model, there is still only one parameter describing the screening effect: it is no longer the ground capacitance C_g but a characteristic length of the long-range Coulomb interaction preventing a divergence of the model, called a_0. In the description of the capacitive effects in our amplifier, we also consider that the chain is terminated by a metallic pad, creating an additional capacitance to ground C_{out} and a shunt capacitance C_s together with the input transmission line [see Fig. 1(a)]. More specifically, the system is modeled by considering the Lagrangian $\mathcal{L}$ of the chain, where the fluxes Φ_n between each SQUID are taken as coordinates. This Lagrangian reads

$$\mathcal{L} = \sum_{n=0}^{N-1} \frac{C_J}{2}(\dot{\Phi}_{n+1} - \dot{\Phi}_n)^2 - \sum_{n=0}^{N-1} \frac{1}{2L_J}(\Phi_{n+1} - \Phi_n)^2 + \sum_{n=1}^{N-1} \frac{C_{g,nn}}{2}\dot{\Phi}_n^2 + \sum_{n=1}^{N-1}\sum_{i\neq n}^{N-1} \frac{C_{g,ni}}{2}(\dot{\Phi}_n^2 - \dot{\Phi}_i^2) + \frac{C_{\text{out}}}{2}\dot{\Phi}_N^2 + \frac{C_s}{2}\dot{\Phi}_N^2 \quad (5)$$

where N is the number of SQUIDs in the chain and $C_{g,ni}$ are the elements of a generalized ground capacitance matrix. We define a new set of variables to describe the

system, the charge Q_n, and its conjugate I_n at each node n:

$$\begin{aligned} Q_n &= \frac{\partial \mathcal{L}}{\partial \dot{\Phi}_n} \\ I_n &= \frac{\partial \mathcal{L}}{\partial \Phi_n}. \end{aligned} \tag{6}$$

These new variables lead to capacitance and inductance matrices ($\hat{C}$ and $\hat{L}$, respectively):

$$\begin{aligned} \vec{Q} &= \hat{C}\dot{\vec{\Phi}} \\ \vec{I} &= \hat{L}^{-1}\vec{\Phi}. \end{aligned} \tag{7}$$

From these matrices, we can define the angular frequency matrix $\hat{\Omega}$ as

$$\hat{\Omega}^2 = -\hat{C}^{-1}\hat{L}^{-1}. \tag{8}$$

The eigenvalues ω_n^2 and eigenvectors of the matrix $\hat{\Omega}^2$ define, respectively, the resonant frequency and the wave profile of each mode n of the chain. It allows the definition of an effective capacitance $C_{\text{eff},n}$ and an effective inductance $L_{\text{eff},n}$ for each mode n:

$$\begin{aligned} C_{\text{eff},n} &= \vec{\varphi}_n^T \hat{C} \vec{\varphi}_n \\ L_{\text{eff},n}^{-1} &= \vec{\varphi}_n^T \hat{L}^{-1} \vec{\varphi}_n. \end{aligned} \tag{9}$$

With this linear model, we now treat the Kerr nonlinearity of the chain. The Josephson nonlinearity can be reintroduced as a perturbation of the linear Hamiltonian, by developing the cosine of the Josephson potential up to fourth order [26]. By applying the rotating wave approximation (RWA), one can rewrite the full Hamiltonian as

$$\begin{aligned} \hat{H} = &\sum_n \hbar\omega_n a_n^\dagger a_n - \sum_n \frac{\hbar}{2} K_{nn} a_n^\dagger a_n a_n^\dagger a_n \\ &- \sum_{n,m} \frac{\hbar}{2} K_{nm} a_n^\dagger a_n a_m^\dagger a_m, \end{aligned} \tag{10}$$

where K_{nn} and K_{nm} are the self- and cross-Kerr coefficients, respectively:

$$\begin{aligned} K_{nn} &= \frac{2\hbar\pi^4 E_J \eta_{nnnn}}{\Phi_0^4 C_J^2 \omega_n^2} \\ K_{nm} &= \frac{4\hbar\pi^4 E_J \eta_{nnmm}}{\Phi_0^4 C_J^2 \omega_n \omega_m}. \end{aligned} \tag{11}$$

η_{nnmm} takes into account the spatial variation of the phase across the chain and $E_J = \varphi_o^2/L_J$ is the Josephson energy of a single SQUID. Given that η_{nnmm} depends only on circuit parameters of the chain, the Kerr nonlinearities of the modes are fully predictable. To describe the effect of the transmission line connected to the array and the resulting external quality factor, we model this $\lambda/4$ resonator as an effective nonlinear series LC circuit [see Fig. 1(b)] close to its resonance. From now on, we drop the index n since we only consider the first mode. Using the effective inductance and capacitance defined previously, we can then easily define an effective resonant frequency $\omega_{\text{eff}} = 1/\sqrt{L_{\text{eff}}C_{\text{eff}}}$, an effective external quality factor $Q_{\text{eff}} = \sqrt{L_{\text{eff}}/C_{\text{eff}}}/Z_c$, and an effective coupling rate $\kappa_{\text{eff}} = \omega_{\text{eff}}/Q_{\text{eff}}$, as is very commonly done in microwave engineering [36]. The accuracy of this mapping relies on a precise determination of the capacitance and inductance matrices. Using a combination of electromagnetic simulations and two-tone measurements, we manage to infer precisely $\hat{C}$ and $\hat{L}$ as will be explained later.

IV. SAMPLE DESCRIPTION

The JPA presented in this work is made of 80 SQUIDs, obtained using a bridge-free fabrication technique [37]. It is fabricated on a 300-μm-thick, single-side-polished, intrinsic silicon wafer. The backside of the wafer is metalized using a sandwich of titanium (10 nm) and gold (200 nm). The array is connected galvanically to a 50 Ω microstrip transmission line on one side and to a superconducting pad on the other side [Fig. 1(a)]. Such a design presents two main advantages. It can be fabricated in one single electronic lithography step and, since no superconducting ground plane is involved, flux-trapping possibilities and the effect of Meissner currents are strongly reduced. The associated circuit parameters are $C_J = 370$ fF, $a_0 = 4.3$ μm, $C_{\text{out}} = 24.7$ fF, and $C_s = 1$ fF. Finally, $L_J = 165$ pH at zero magnetic flux, which translates into a critical current of $I_c = 2$ μA for each SQUID. L_J remains larger than the kinetic inductance of the aluminum wires connecting the SQUIDs. We estimate this stray inductance to be $L_{\text{stray}} = 30$ pH. Ensuring $L_{\text{stray}} \ll L_J$ is important to the validity of our model [Fig. 1(b)]. C_J is inferred via the size of the junctions and the capacitance density 45 fF/μm^2 [38]. The values of C_{out} and C_s are obtained using electromagnetic simulation software. L_J and a_0 are determined from the dispersion relation of the array, as explained in Sec. V.

V. CHARACTERIZATION IN THE LINEAR REGIME

The device is measured using a conventional cryogenic microwave measurement setup (see Appendix A). The linear properties of the JPA are inferred by measuring the reflected phase of the microwave signal at zero flux and low power [Fig. 3(c)]. The fit of the phase shift yields

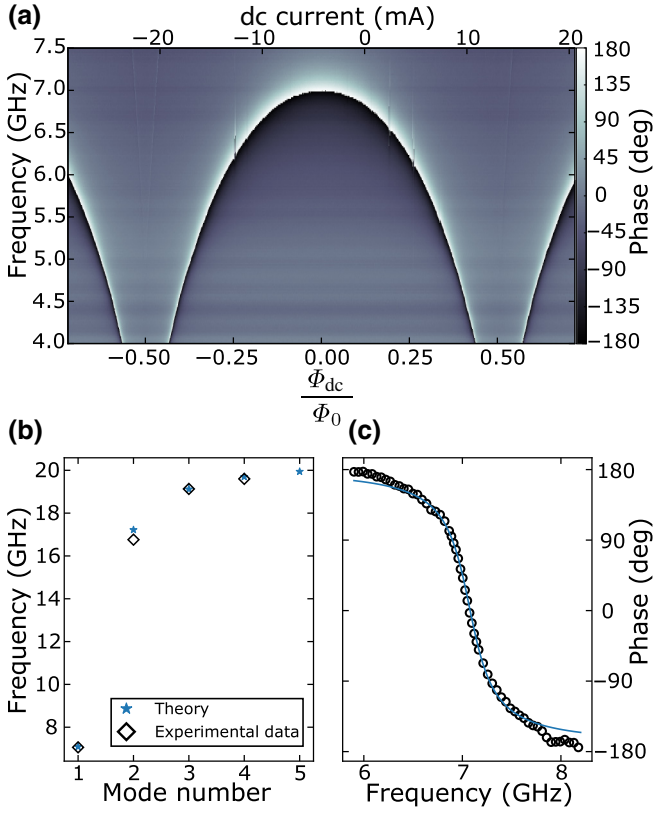

FIG. 3. (a) dc flux modulation of the phase of the reflected signal. (b) Dispersion relation of the SQUID array for the first modes. Blue stars are the solution of the matrix computation and black diamonds show experimental data. (c) Cut of (a) at zero magnetic flux, where the experimental data are fitted by an arctangent.

$\omega_{exp}/2\pi = 7.07$ GHz and $Q_{exp} = 19$. The resonant frequency of the JPA can be adjusted over a broad frequency range when flux-biasing the SQUID array [Fig. 3(a)]. We note the smooth behavior of the device during flux tuning, despite the presence of the SQUID array. We attribute this stability to the absence of the superconducting ground plane. We can go one step further in the characterization of the device and obtain the dispersion relation of the array using two-tone spectroscopy [34,39]. The higher-order resonant frequencies of the device are presented in Fig. 3(b). Fitting these data using the circuit model presented in Sec. III, we can determine L_J and a_0 independently. Plugging these values into the effective model introduced before, we obtain the values $L_{eff} = 21$ nH, $C_{eff} = 24$ fF, and $K_{eff} = 80$ kHz. These values translate to an effective resonant frequency $\omega_{eff}/2\pi = 7.08$ GHz and an effective external quality factor $Q_{eff} = 19$ in very good agreement with the measured values. We note that this external quality factor is much smaller than internal quality factors $Q_{int} \sim 10^4$ that we measured in devices fabricated using the same procedure [26]. This result justifies that internal losses can be safely neglected in our model. In the next section, we will use the value of K_{eff} to explain the measured gain, bandwidth, and 1-dB compression point of the JPA without any free parameters.

VI. GAIN AND INPUT SATURATION POWER

In Fig. 4(a), we present the gain of the amplifier versus frequency at various pump powers. We measure a −3-dB bandwidth of $\Delta f = 45$ MHz at 20 dB of gain. All these gain curves can be explained by Eq. (3) using only the above-mentioned effective parameters. Interestingly, it also provides an accurate calibration of the pump power at the JPA level and thus of the attenuation of the input line (see Appendix F). We note that our JPA can be flux tuned over a band of 900 MHz while reaching $G_{max} = 20$ dB, as shown in Appendix C. Knowing the attenuation of the input line, the input saturation power of the JPA is quantified by measuring the maximum gain G_{max} as

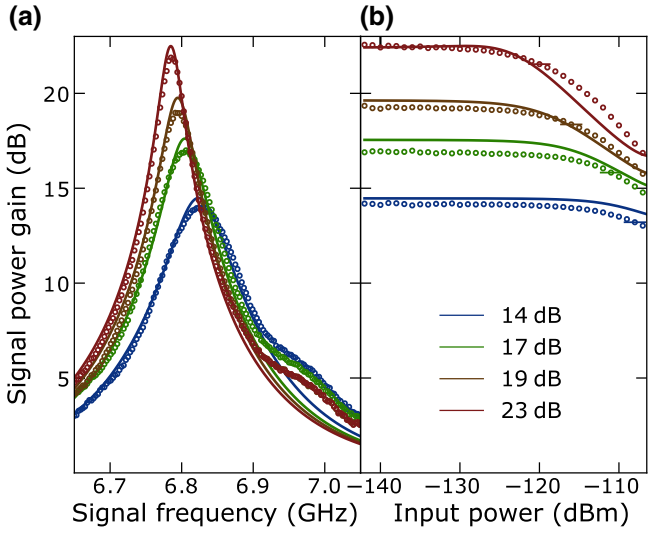

FIG. 4. (a) Signal power gain versus signal frequency, with experimental (dotted lines) and calculated (solid lines) gain at four different pump powers and frequencies. The theoretical pump parameters are chosen as follows: the pump frequency is first set to the one used experimentally. The pump power is then set to maximize the gain at zero detuning ($\Delta = 0$), as done experimentally. This process leads to optimal pump biasing conditions, which can be visualized as the ridge on Fig. 2. These optimal conditions are (from low gain to high gain) (−81.65 dBm, 6.83 GHz); (−81.12 dBm, 6.80 GHz); (−80.83 dBm, 6.79 GHz); (−80.57 dBm, 6.78 GHz). The bumps on the right tail of the experimental amplification curves are due to the normalization procedure and small losses at zero pump power. (b) Maximum gain as a function of the input power signal for the four same pump parameters. The pump powers for the theoretical plots have been shifted by up to ±0.03 dBm from the optimal pump power to account for the fact that a very small variation of pump power translates in a large variation of the gain as explained in the text. Such shifts are compatible with small drifts in the attenuation of the input line over the course of one day.

a function of input power for different gains [Fig. 4(b)]. More specifically, we measure a 1-dB compression point $P_{1\mathrm{dB}} = -117 \pm 1.4$ dBm at 20 dB of gain. This point corresponds to the input power at which the amplifier saturates and the gain is compressed by 1 dB from $G_{\max}$. Again, we show a very good agreement between experiment and theory, without fitting parameters. To describe the saturation of the JPA, the number of signal photons inside the JPA must be taken into account while the pump is on. To do so, we add, in a self-consistent approach [14], the terms $2iK\langle a^\dagger a\rangle\alpha$ and $iK\langle a^2\rangle\alpha^*$ to the initial equation of motion of the intraresonator field (see Appendix E). This correction to the total number of photons inside the cavity (pump, signal, and idler), dependent on the signal power, allows the modeling of the amplifier saturation for a given set of pump frequencies and powers as plotted in Fig. 4(b). As will be explained in the next section, this saturation is very sensitive to the pump biasing conditions.

VII. DISCUSSION

To further illustrate the performance of our device and the predictive value of our model, we summarize three important figures of merit of our JPA in Fig. 5. These are the maximum gain, the −3-dB bandwidth, and the 1-dB compression point. The maximum gain $G_{\max}$ at low signal power and the corresponding −3-dB bandwidth Δf are measured for different pump powers [panels (a) and (b)]. The gain-bandwidth product remains equal to 450 MHz over this pump power range, as expected from JPA theory. We now compare the 1-dB compression points measured at various gains to our theoretical predictions. Such a plot should be interpreted with great care since a very small deviation from optimal pump conditions can lead to variations of P_{1dB} as reported previously [17]. For example, a pump power variation of 0.03 dBm leads to a change of up to 3 dBm in $P_{1\mathrm{dB}}$, as illustrated by the shaded area of Fig. 5(c). To illustrate the advantage of using SQUID arrays, we also plot what would be$P_{1\mathrm{dB}}$ for a single SQUID JPA as reported in various papers [6,40]. To ensure a meaningful comparison, we choose the parameters of this single SQUID JPA so that it displays the same working frequency ($\omega_{\mathrm{exp}}/2\pi = 7.07$ GHz) and bandwidth ($Q_{\mathrm{exp}} = 19$) as our array JPA. The self-Kerr coefficient of such a JPA would be $K_{\mathrm{single}}/2\pi = 2.4$ MHz (to be compared to $K_{\mathrm{eff}}/2\pi = 80$ kHz). This result translates into $P_{1\mathrm{dB,single}} = -131$ dBm at $G_{\max} = 20$ dB compared to $P_{1\mathrm{dB,array}} = -116$ dBm for our array JPA. This 15-dBm difference reflects directly the ratio of self-Kerr coefficients since $P_{1\mathrm{dB}}$ scales as $\kappa_{\mathrm{eff}}/|K_{\mathrm{eff}}|$, as explained previously. This result illustrates the key advantage of using arrays to fabricate high-performance JPAs. Finally, we would like to discuss the data/theory agreement. According to our microscopic model, $P_{1\mathrm{dB}}$ should be −116 dBm, while we measured -117 ± 1.4dBm. This good agreement confirms that adding two terms to the equation of motion of the intraresonator field is enough to explain the saturation effect observed in our JPA. From a physical point view, the effect of these terms is twofold. First, the bare frequency of the JPA ω_{eff} becomes dependent on the number of signal photons, similarly to the ac-Stark shift effect. Second, the number of pump photons inside the JPA depends as well on the number of signal photons, an effect known as pump depletion in parametric amplifier theory.

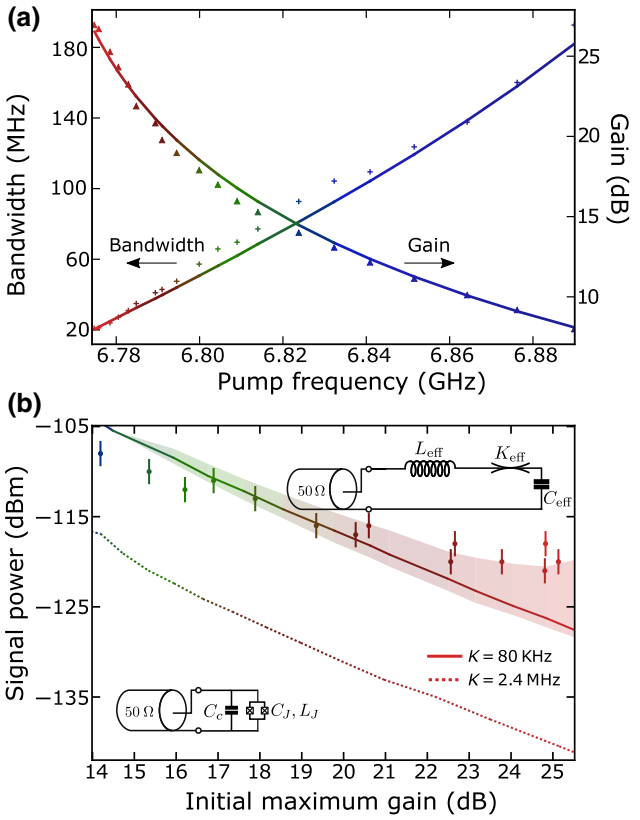

FIG. 5. Summary of the amplifier characteristics and agreement between experiment (dotted line) and theory for optimal pumping condition (solid line). (a) Maximum gain and −3-dB bandwidth (obtained from a Lorentzian fit of the amplification curve) as a function of the pump frequency. The gain theoretical line follows the highlighted ridge shown in Fig. 2(b). (b) 1-dB compression point as a function of the initial maximum gain. The shaded area below (above) the theoretical curve shows the effect of a shift of +0.03 dBm (−0.03 dBm) from the optimal pump power on the 1-dB compression point. The dashed line shows the 1-dB compression point of a single-SQUID JPA, which would show the same bandwidth and operating frequency.

VIII. CONCLUSION

We design and measure a Josephson parametric amplifier made of 80 SQUIDs. This device relies on a single-step, all-aluminum fabrication process, easily reproducible in a research-grade cleanroom. We showed that the number

of SQUIDs in the array has a direct and predictable impact on the nonlinearity, which is directly linked to the saturation power of the amplifier. The circuit model we use gives a very good agreement with the experimental data, without fitting parameters. Improvements could be obtained by bringing the Josephson inductance down to $L_J \approx L_{\text{stray}}$. Setting L_J to 40 nH, just above L_{stray}, adjusting C_{out} to 50 fF and the total number of SQUIDs to $N = 150$, would lead to a JPA with a bare resonant frequency $f_0 = 7.45$ GHz and external quality factor $Q_e = 9$. According to our model, this JPA would display for a 20-dB signal gain, a bandwidth of 95 MHz, and a 1-dB compression point of -102 dBm. A pump power of -66 dBm would be necessary to operate a JPA with these figures of merit. This value is comparable to what was reported for Josephson traveling wave parametric amplifier [41,42] and, as such, should not be a concern. We would like to stress that these estimates cannot be strictly quantitative since the approximation described in Sec. IV ($L_{\text{stray}} \ll L_J$) does not hold anymore. Theory should be further developed to account for the effect of these stray inductances. Further developments that could be applied to this SQUID array JPA include input impedance engineering to improve the performance of the device [1,2] or band engineering to bring in new capabilities such as nondegenerate [4] or multimode parametric amplification [43].

ACKNOWLEDGMENTS

The authors would like to thank W. Wernsdorfer, E. Eyraud, F. Balestro, and T. Meunier for early support with the experimental setup. Very fruitful discussions with F. W. Hekking, D. Basko, and I. Takmakov are strongly acknowledged. This research is supported in part by the International Centre for Theoretical Sciences (ICTS) during a visit for participating in the program Open Quantum Systems (Code: ICTS/Prog-oqs2017/2017/07). This research is supported by the ANR under contracts CLOUD (Grant No. ANR-16-CE24-0005). J.P.M. acknowledges support from the Laboratoire d'Excellence LANEF in Grenoble (Grant No. ANR-10-LABX-51-01). R.D. and S.L. acknowledge support from the CFM foundation.

APPENDIX A: EXPERIMENTAL SETUP

The full measurement setup is shown in Fig. 6. The device is placed in a dilution refrigerator at a base temperature of 20 mK and the transmission measurements are performed using a vector network analyzer (VNA). An additional microwave source is used for two-tone measurements, while a global magnetic field is applied via an external superconducting coil. The output line includes one isolator at 20 mK, a high electron mobility transistor (HEMT) amplifier at 4 K, and room-temperature amplifiers. The input line is attenuated at various stages, including a home-made filter that prevents stray radiation from reaching the sample. We adopted a coaxial geometry with a dissipative dielectric (reference RS-4050 from Resin Systems Company). The bandwidth of the measurement setup goes from 4 to 13 GHz.

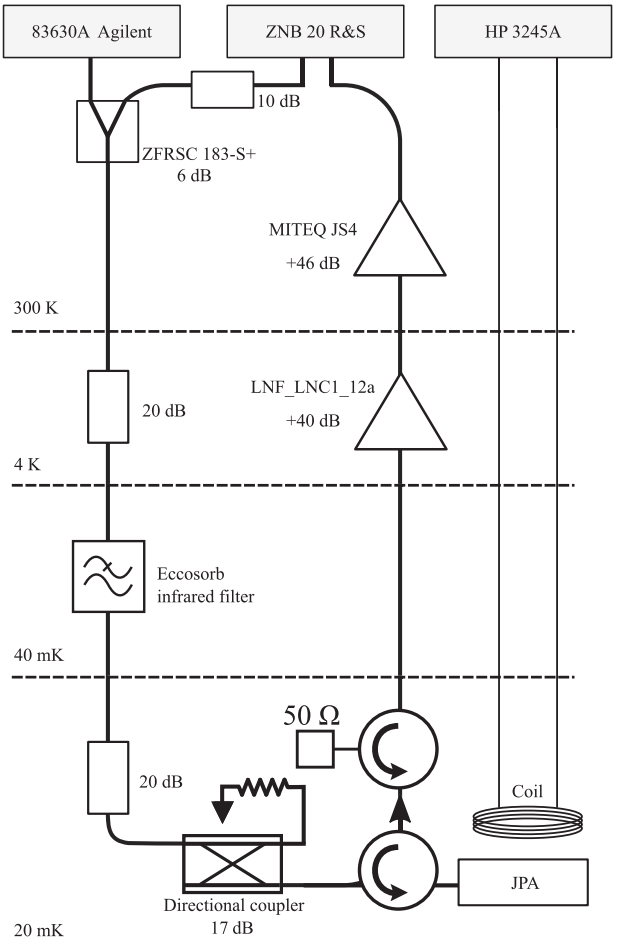

FIG. 6. Experimental setup.

APPENDIX B: DILUTING THE NONLINEARITY IN A JOSEPHSON ARRAY

In this appendix, we briefly demonstrate the effect of an array of Josephson junctions on the effective nonlinearity. For the sake of simplicity, we do not take into account the propagation effects. First, we start to derive an expression for the nonlinearity for a single junction whose Hamiltonian is

$$\hat{H} = \frac{\hat{Q}^2}{2C} + E_J \cos\hat{\varphi}, \tag{B1}$$

where $\hat{Q}$ is the charge operator and $\hat{\varphi}$ is its conjugate such as $[\hat{Q}, \hat{\varphi}] = -2ie$, with e the positive charge of the electron. C is the capacitance of the junction. $E_C = q/2C$ and E_J are the charging and the Josephson energy of the junction, respectively, defining the resonance frequency of the

junction $\hbar\omega_o = \sqrt{8E_J E_C}$. Under the assumption that the phase fluctuations are small, the cosine potential is developed up to the fourth order: $E_J \cos\hat{\varphi} = E_J - E_J\hat{\varphi}^2/2! + E_J\hat{\varphi}^4/4! + o(\hat{\varphi}^4)$. Then $\hat{q}$ and $\hat{\varphi}$ are written as a function of creation and annihilation operators:

$$\hat{q} = q_{\text{zpf}}(\hat{a}^\dagger + a) \tag{B2a}$$

$$\hat{\varphi} = i\varphi_{\text{zpf}}(\hat{a}^\dagger - a), \tag{B2b}$$

where zpf stands for zero point fluctuations, with $q_{\text{zpf}} = \sqrt{\hbar\omega C/2}$ and $\varphi_{\text{zpf}} = \sqrt{\hbar/2C\omega} \propto (E_C/E_J)^{1/4}$. The Hamiltonian is rewritten as

$$\hat{H} = \frac{1}{2C}q_{\text{zpf}}^2(\hat{a}^\dagger + a)^2 + \frac{E_J}{2}\varphi_{\text{zpf}}^2(\hat{a}^\dagger - a)^2 - \frac{E_J}{4!}\varphi_{\text{zpf}}^4(\hat{a}^\dagger - a)^4. \tag{B3}$$

The last term on the right-hand side of Eq. (B3) is the nonlinearity linked to the self-Kerr coefficient by $K = E_J\varphi_{\text{zpf}}^4/4!\hbar \propto E_C/\hbar$ [44].

Let us consider now the N series junctions case. The Josephson potential is written $NE_J \cos(\hat{\varphi}/N)$, under the assumption that the phase drop across the chain is equally divided across each junction. The potential is once again developed to the fourth order $NE_J \cos(\hat{\varphi}/N) = NE_J - NE_J\hat{\varphi}^2/2N^2 + NE_J\hat{\varphi}^4/4!N^4$. The second term is simplified in $E_J\hat{\varphi}^2/2N$ and a new Josephson energy is defined as $E_J^* = E_J/N$. Considering that we want to keep the same resonance frequency, it leads to

$$\hbar\omega_0 = \sqrt{8E_C E_J} = \sqrt{8E_C^* E_J^*} \tag{B4}$$

This condition gives $E_C^* = NE_C$ and leads to $\varphi_{ZPF}^* \propto (E_C^*/E_J^*)^{1/4} \propto N^{1/2}(E_C/E_J)^{1/4} \sim N^{1/2}\varphi_{ZPF}$. Now the new Kerr term K^* is

$$\hbar K^* = \frac{NE_J}{4!}\frac{{\varphi_{ZPF}^*}^4}{N^4} = \frac{E_J}{4!}\varphi_{ZPF}^4\frac{1}{N} = \frac{\hbar K}{N}. \tag{B5}$$

We demonstrate that with an array of N Josephson junctions, while keeping the same resonance frequency and under the assumption that each junction is equally phase-biased in the array, the nonlinearity is divided by N compared to the single junction case. This calculation is only meant to give a qualitative estimation since, in a real device, propagating effects have to be accounted for, as explained in the main text.

APPENDIX C: FLUX TUNABILITY

In this section, we show the frequency range on which the amplification is possible while flux tuning the array. In the main text, we present the flux tunability of the JPA by showing the 2π phase shift from 7 to 4 GHz, which corresponds to the bare frequency of the array and the lower bound of the circulator, respectively. Nonetheless, this frequency window does not correspond to the band on which amplification is reachable. We arbitrarily define the range of effective tunability as the range where 20-dB signal gain can be observed. We show in Fig. 7 signal gain for different dc flux biasing. We could obtain clear amplification from approximately 6.8 GHz ($\Phi = 0\Phi_0$) to 5.9 GHz ($\Phi \approx 0.25\Phi_0$). At lower frequencies, the critical current of the SQUID decreases too much compared to the pump current necessary to achieve a 20-dB gain.

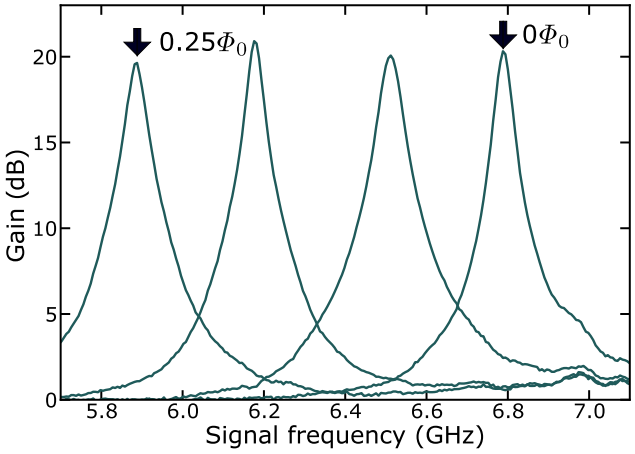

FIG. 7. Gain of the amplifier for different flux bias configurations.

APPENDIX D: REMOTE GROUND MODEL

In Table I, we compare four SQUID array models to experimental results and justify our choice to use the remote ground model, as described in Sec. III of the main text. The simplest way to model such an array is to only consider the Josephson inductances L_J and the capacitances C_{out} and C_s, without taking into account the capacitive effect between the SQUIDs and the ground. With this oversimplified model, we can choose L_J to obtain the right resonant frequency but the value of the quality factor is then wrong and vice versa. Moreover, no propagating effects can be described and thus the dispersion relation cannot be reproduced. The standard model using a ground capacitance C_g for each elementary cell (local screening of the charge Q_n by the ground) can reproduce the dispersion relation, but the values of the external quality factor and resonant frequency are less accurate. Finally, the remote ground model reproduces well the dispersion relation and returns an effective quality factor Q_{eff} closer to the experimental one. An intuitive way to estimate the effective parameters of the circuit without going through the matrix computation shown in the main text is to take C_{out}, C_J, and C_s equal to zero and consider the array as

TABLE I. Comparison of the effective parameters between three models of the SQUID array and the parameters found experimentally.

	f_{eff} (GHz)	Q_{eff}	K_{eff} (KHz)
Experimental	7.07	19	x
No ground capacitance	7.95	13	98
Ground capacitance	7.05	21	80
Remote ground	7.08	19	80
$\frac{\lambda}{4}$ resonator	7.07	12	x

a simple transmission line. Then each unitary cell has an inductance L_J, a ground capacitance C_g, and an impedance $Z_{\text{TL}} = \sqrt{L_J/C_g}$. In that case, there is a direct mapping between a $\lambda/4$ resonator and an effective LC series resonator close to resonance [36]. We can define an effective inductance and an effective capacitance as

$$L_{\text{eff,TL}} = \frac{\pi Z_{\text{TL}}}{4\omega_0} \tag{D1a}$$

$$C_{\text{eff,TL}} = \frac{1}{\omega_0^2 L_{\text{eff,TL}}}. \tag{D1b}$$

By setting the first resonance to $\omega_0/2\pi = 7.07$ GHz and L_J and C_g to the values inferred from the measured dispersion relation (165 pH and 0.3 fF, respectively), we find a characteristic impedance $Z_c = \sqrt{L_{\text{eff,TL}}/C_{\text{eff,TL}}} = 600\ \Omega$. The external quality factor is then given by $Q_{\text{eff,TL}} = Z_c/Z_0 = 12$. This oversimplified model fails to reproduce, at the same time, the experimental values of the resonant frequency and the external quality factor. In the following table, we present the different effective parameters found (ω_{eff}, Q_{eff}, and K_{eff}) using the various models, as well as the experimental values.

APPENDIX E: DERIVATION OF THE GAIN

In this section, we detail the derivation to obtain the expression of the gain, as a function of the pump and signal parameters. As in the main text, we start by describing the circuit with the Hamiltonian of a nonlinear resonator with annihilation and creation operators:

$$H_{\text{JPA}} = \hbar\omega_{\text{eff}} A^\dagger A + \hbar\frac{K_{\text{eff}}}{2}\left(A^\dagger\right)^2 A^2. \tag{E1}$$

The dynamics of the circuit is described with the conventional input-output theory:

$$\dot{A} = -i\omega_{\text{eff}} A - iK_{\text{eff}} A^\dagger AA - \frac{\kappa_{\text{eff}}}{2}A + \sqrt{\kappa_{\text{eff}}}A_{\text{in}}. \tag{E2}$$

We neglect the internal losses as they are much smaller than the coupling rate κ_{eff}. In this derivation, the intraresonator field $A(t) = (\alpha + a(t))e^{i\omega t}$ is decomposed in two components: a strong, classical field $\alpha e^{i\omega t}$ called pump and a weak, quantum field $a(t)$, which we refer to as the signal. First, Eq. (E2) is considered only with the pump field $A(t) = \alpha(t)e^{i\omega t}$. We multiply both sides with their complex conjugate, leading to

$$1 = \left(\delta^2 + \frac{1}{4}\right)n - 2\delta\xi_\alpha n^2 + \xi_\alpha^2 n^3, \tag{E3}$$

where $\delta = (\omega_p - \omega_{\text{eff}})/\kappa_{\text{eff}}$ is the detuning between the pump and the bare frequency of the resonator, $\tilde{\alpha}_{\text{in}} = \alpha_{\text{in}}/\sqrt{\kappa_{\text{eff}}}$ is the dimensionless drive amplitude, $\xi_\alpha = |\tilde{\alpha}_{\text{in}}|^2 K_{\text{eff}}/\kappa_{\text{eff}}$ is the pump strength, and finally $n = |\alpha|^2/|\tilde{\alpha}_{\text{in}}|^2$ is the mean number of pump photons inside the nonlinear resonator. We numerically solve this equation, which is cubic in n, to determine the number of pump photons as a function of the pump power and pump frequency. Once this equation solved, the signal tone is added [$A(t) = \alpha(t) + a(t)$], Eq. (E2) is linearized for the weak quantum signal, and only the first-order terms in $a(t)$ are kept:

$$\dot{a}(t) = i\left(\omega_p - \omega_{\text{eff}} - 2K_{\text{eff}}|\alpha|^2 + i\frac{\kappa_{\text{eff}}}{2}\right)a(t) - iK_{\text{eff}}\alpha^2 a^\dagger(t) + \sqrt{\kappa_{\text{eff}}}a_{\text{in}}. \tag{E4}$$

To solve Eq. (E4), $a(t)$ is decomposed into its Fourier components since Eq. (E4) is linear in $a(t)$:

$$a(t) = \frac{\kappa_{\text{eff}}}{\sqrt{2\pi}}\int_{-\infty}^{\infty} a_\Delta d\Delta e^{-i\Delta\kappa_{\text{eff}}t}, \tag{E5}$$

where $\Delta = (\omega_s - \omega_p)/\kappa_{\text{eff}}$ is the dimensionless detuning between the pump and the signal. Equation E4 can be rewritten as a function of the Fourier components of $a(t)$, using the parameters defined before:

$$0 = \left(i(\delta - 2\xi_\alpha n + \Delta) - \frac{1}{2}\right)a_\Delta - i\xi_\alpha n e^{2i\phi}a^\dagger_{-\Delta} + \tilde{a}_{\text{in},\Delta}. \tag{E6}$$

Since Eq. (E4) mixes a_Δ and its conjugate $a^\dagger_{-\Delta}$, the conjugate of Eq. (E4) has to be accounted for to have a full expression of a_Δ as a function of the dimensionless input $\tilde{a}_{\text{in},\Delta} = a_{\text{in},\Delta}/\sqrt{\kappa_{\text{eff}}}$ and its conjugate $\tilde{a}^\dagger_{\text{in},\Delta} = a^\dagger_{\text{in},\Delta}/\sqrt{\kappa_{\text{eff}}}$. This leads to a set of two equations linking input and output, which can be written as a matrix equation:

$$\begin{pmatrix}\tilde{a}_{\text{in},\Delta}\\ \tilde{a}^\dagger_{\text{in},-\Delta}\end{pmatrix} = \begin{pmatrix} i(-\delta + 2\xi_\alpha n - \Delta) + \frac{1}{2} & i\xi_\alpha n e^{-i2\phi} \\ -i\xi_\alpha n e^{-i2\phi} & i(\delta - 2\xi_\alpha n - \Delta) + \frac{1}{2}\end{pmatrix} \times \begin{pmatrix} a_\Delta \\ a^\dagger_{-\Delta}\end{pmatrix}. \tag{E7}$$

By inverting the matrix, we can have access to the expression of a_Δ and $a^\dagger_{-\Delta}$ as a function of the input field $\tilde{a}_{\text{in},\Delta}$ and $\tilde{a}^\dagger_{\text{in},-\Delta}$ and the pump parameter δ, ξ_α, n, and Δ:

$$a_\Delta = \frac{i(\delta - 2\xi_\alpha n - \Delta) + \frac{1}{2}}{(i\Delta - (\frac{1}{2} - \sqrt{(\xi_\alpha n)^2 - (\delta - 2\xi_\alpha n)^2}))(i\Delta - (\frac{1}{2} + \sqrt{(\xi_\alpha n)^2 - (\delta - 2\xi_\alpha n)^2}))}\tilde{a}_{\text{in},\Delta} + \frac{-i\xi_\alpha n e^{2i\phi}}{(i\Delta - (\frac{1}{2} - \sqrt{(\xi_\alpha n)^2 - (\delta - 2\xi_\alpha n)^2}))(i\Delta - (\frac{1}{2} + \sqrt{(\xi_\alpha n)^2 - (\delta - 2\xi_\alpha n)^2}))}\tilde{a}^\dagger_{\text{in},-\Delta}. \tag{E8}$$

Finally, we can link the intracavity field a_Δ with the output field with the boundary condition:

$$a_{\text{out},\Delta} = \sqrt{a_\Delta} - a_{\text{in},\Delta}, \tag{E9}$$

leading to an expression linking the output field to the input field:

$$a_{out,\Delta} = -1 + \frac{i(\delta - 2\xi_\alpha n - \Delta) + \frac{1}{2}}{(i\Delta - \lambda_-)(i\Delta - \lambda_+)}\tilde{a}_{\text{in},\Delta} + \frac{-i\xi_\alpha n e^{2i\phi}}{(i\Delta - \lambda_-)(i\Delta - \lambda_+)}\tilde{a}^\dagger_{\text{in},-\Delta}, \tag{E10}$$

with $\lambda_\pm = \frac{1}{2} \pm \sqrt{[(\xi_\alpha n)^2 - (\delta - 2\xi_\alpha n)]}$. Signal and idler gains are defined as the ratio between the output field and input field at Δ and $-\Delta$, respectively. We can define the signal gain as the prefactor of $\tilde{a}_{\text{in},\Delta}$ in Eq. (E10), as in the main text. The maximum gain at zero detuning between the pump and the signal ($\Delta = 0$) as a function of the pump power and pump frequency is plotted in Fig. 2 with our JPA parameters.

Gain versus signal-pump detuning is plotted in Fig. 2. Theory and experimental points are obtained following the same protocol: for a given pump frequency (the same for theory and experiment), the pump power is set to obtain the maximal signal gain at $\Delta = 0$, with no regard for other parameters. By comparing the experimental, injected pump power and the theoretical, expected one, we are able to make a calibration of the input line (see Appendix F). Up to now, the mean number of signal photons is set to 0. To go further in our understanding of the JPA, the saturation is modeled by taking into account the number of signal photons inside the nonlinear cavity. To take into account this number, the terms $2iK\langle a^\dagger a\rangle\alpha$ and $iK\langle a^2\rangle\alpha^*$, previously neglected, are now added to Eq. (E2). Following the same mathematical steps with these two new terms, we obtain a new cubic equation in n, the mean number of photons inside the cavity, now depending not only on pump parameters but also on the input signal power:

$$1 = n\{\delta^2 + \frac{1}{4} - 4\xi_a\delta + 5\xi_a^2 + \xi_a[(2\xi_a^2 + \delta)\cos 2\Delta\phi + \frac{1}{2}\sin 2\Delta\phi]\} + n^2(-2\delta\xi_\alpha + 4\xi_\alpha\xi_a + \xi_\alpha\xi_a\cos 2\Delta\phi) + n^3\xi_\alpha^2, \tag{E11}$$

where $\xi_a = K_{\text{eff}}n_a/\kappa_{\text{eff}}$ is the normalized signal strength, n_a is the mean photon number created by the input signal power $n_a = \langle a^\dagger_\Delta a_\Delta\rangle + \langle a^\dagger_{-\Delta}a_{-\Delta}\rangle$, and $\Delta\phi$ the phase difference between the pump and the signal. To consider the terms depending on $\Delta\phi$ (operating in phase-sensitive mode), the difference between the signal frequency and the pump frequency has to be smaller than the IF bandwidth. Otherwise, these terms average to 0. Given the IF bandwidth $\kappa_{\text{if}} = 10$ Hz used in our experiment, these terms can be safely neglected. We link n_a to the input power using Eq. (E8), giving the intracavity field as a function of the input power. Moreover, we neglect the idler input power $\tilde{a}^\dagger_{\text{in},-\Delta}$ and the associated vacuum fluctuations, which leads to

$$a_\Delta = \frac{i(\delta - 2\xi_\alpha n - \Delta) + \frac{1}{2}}{(i\Delta - \lambda_-)(i\Delta - \lambda_+)}\tilde{a}_{\text{in},\Delta} \tag{E12a}$$

$$a^\dagger_{-\Delta} = \frac{i\xi_\alpha n e^{2i\phi}}{(i\Delta - \lambda_-)(i\Delta - \lambda_+)}\tilde{a}_{\text{in},\Delta} \tag{E12b}$$

where $|\tilde{a}_{\text{in},\Delta}|^2 = P_{\text{signal}}/\hbar\omega_s\kappa_{\text{eff}}$. Using this formula, we compute the photon number inside the cavity while taking into account the signal power and the Kerr shift induced by the signal power. We set the pump parameters to reach the optimal maximum gain (as explained in the previous paragraph), while $\Delta = 0$. We observe a decrease in the gain as the signal power increases, as shown in the main text in Fig. 3(b). Since this mean-field approach needs to be solved self-consistently, once this new pump photon number n [the solution of Eq. (E11)] is obtained, n has to be plugged again into Eq. (E8) to get the actual number of signal photons inside the cavity, which will affect the pump photon number inside the cavity and so on. We iterate this loop several times and show in Fig. 8 that the saturation process converges after four iterations. In this study, the input power of the quantum fluctuations has not been taken into consideration in the calculation of the mean photon number n_a. Care has been taken to ensure that saturation of the amplifier starts for n_a greater than 1, which means that the input power of the quantum fluctuations is negligible in the saturation. Nonetheless, in the calculation of the 1-dB compression point for a Kerr constant equal to 2.4 MHz in the main text, saturation occurs for n_a smaller than 1 for gain greater than 20 dB. This result means that quantum fluctuations themselves saturate the amplifier. A model taking into account these fluctuations in a self-consistent way is beyond the scope of this paper.

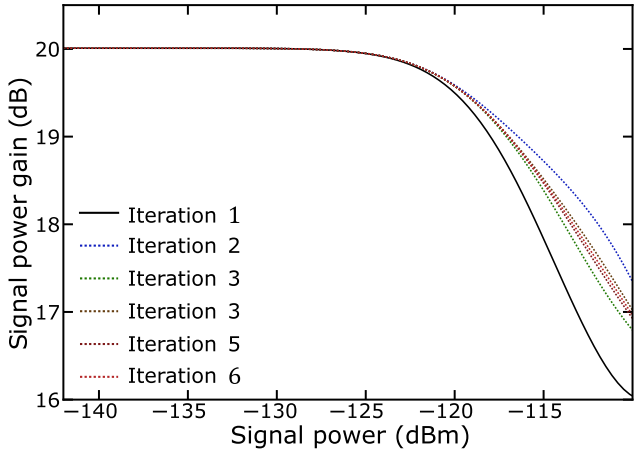

FIG. 8. Maximum gain as a function of the input signal power, where the actual number of signal photons inside the resonator is being iteratively computed five times.

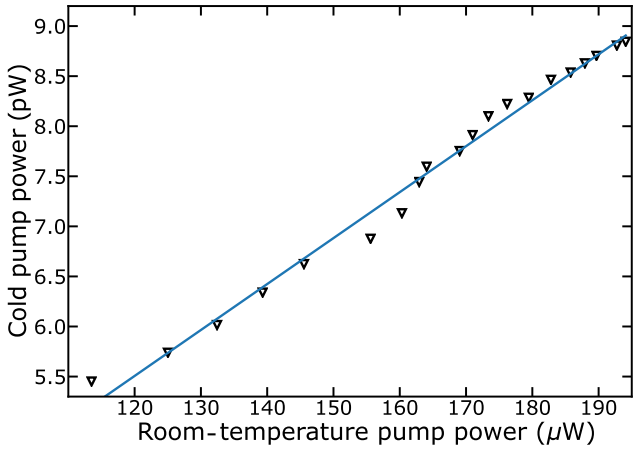

FIG. 9. Power at the input of the JPA versus room temperature power.

APPENDIX F: CALIBRATION OF THE INPUT LINE

In this section, we detail how the calibration of the input is done. To do so, we plug our JPA characteristics (resonant frequency, bare bandwidth, and nonlinearity) into the model detailed in the last section. As explained, we compare the amplification process (by sweeping the signal frequency around the pump frequency) between theory and experimental data for several pump sets. To choose a set of pump parameters, we follow the same protocol for both theory and experimental data: once the pump frequency is fixed, we look for the pump power leading to the greater gain at $\Delta = 0$. Considering the predictability of the model [see Figs. 3(a) and 3(b)], we compare experimental, room-temperature power at the output of the pump source with theoretical power at the input of the JPA. We plot in Fig. 9 points whose ordinate is the theoretical power and whose abscissa is the experimental one. We fit these points with a linear relation, whose the intercept is 0 and the slope is -73.4 dB. We set the total attenuation between the pump output and the JPA input to -73.0 dB. This calibration is consistent with the 63 dB of discrete attenuators between the pump output and the JPA, and with $7\ \mathrm{dB/m} \times 1.5\ \mathrm{m} + 3\ \mathrm{dB/m} \times 0.4\ \mathrm{m} = 11.7$ dB of attenuation across the different cables (see Fig. 6). Therefore, there is a discrepancy of 1.4 dB between our calibration based on the self-Kerr effect and our estimation based on the characteristics of the cables. We use this difference to set the size of the error bars in our measurements.

APPENDIX G: NOISE PROPERTIES OF THE AMPLIFIER

We discuss here the noise properties of a JPA nominally identical to the one presented in this paper. The analysis is closed to the one described in Appendix B of the Lin *et al.* paper [45]. We measure the power spectral density (PSD) at the output of the whole measurement chain when the JPA is off and compare it to the case where it is operated with finite gain. This measurement chain consists of a JPA followed by a HEMT amplifier[Fig. 10(a)]. Inevitable losses η are present between the JPA and the HEMT amplifier. They are mainly caused by the insertion losses of various microwave components such as circulators, for example, all thermalized at the same temperature as the JPA (T_{in}). At a given pump frequency ω_p, the power spectral density when the JPA is off is given by

$$\mathrm{PSD}_{\mathrm{off}} = G_{\mathrm{HEMT}} k_B (T_{\mathrm{HEMT}} + T_{\mathrm{in}}) \simeq k_B T_{\mathrm{HEMT}}. \tag{G1}$$

We assume that the input of the JPA is connected to a perfect 50-Ω resistance giving a vacuum noise of half a photon, $T_{\mathrm{in}} = \hbar\omega_p / 2k_B = 166$ mK. We assume as well that the HEMT amplifier is the main source of noise in this case.

When the JPA is operated with a gain G_{JPA}, the PSD increases because of the contribution of the amplified added noise of the JPA, $G_{\mathrm{JPA}}(1-\eta)k_B T_{\mathrm{JPA}}$, with T_{JPA} the effective noise temperature of the JPA. The total PSD is then given by

$$\mathrm{PSD}_{\mathrm{on}} = G_{\mathrm{HEMT}} k_B [T_{\mathrm{HEMT}} + G_{\mathrm{JPA}}(T_{\mathrm{JPA}} + T_{\mathrm{in}})(1-\eta) + \eta T_{\mathrm{in}}] \tag{G2}$$

where we suppose that the noise of the JPA does not depend on its gain.

Therefore, the PSD ratio, R_{PSD} is

$$\begin{aligned} R_{\mathrm{PSD}} &= \frac{\mathrm{PSD}_{\mathrm{on}}}{\mathrm{PSD}_{\mathrm{off}}} \\ &= \frac{T_{\mathrm{HEMT}} + \eta T_{\mathrm{in}}}{T_{\mathrm{HEMT}} + T_{\mathrm{in}}} + G_{\mathrm{JPA}}(1-\eta)\frac{T_{\mathrm{JPA}} + T_{\mathrm{in}}}{T_{\mathrm{HEMT}} + T_{\mathrm{in}}} \\ &\simeq 1 + G_{\mathrm{JPA}}(1-\eta)\frac{T_{\mathrm{JPA}} + T_{\mathrm{in}}}{T_{\mathrm{HEMT}}}. \end{aligned} \tag{G3}$$

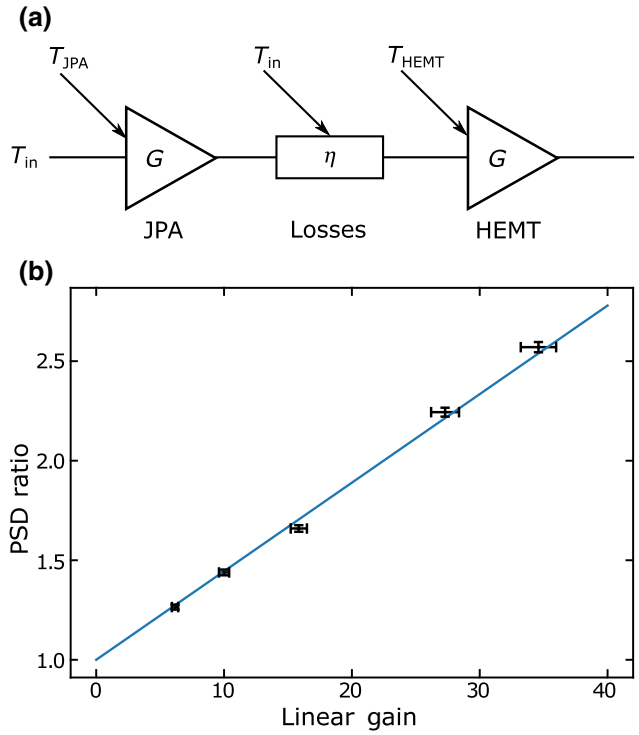

FIG. 10. (a) Simplified diagram of the amplification chain. (b) PSD ratio as a function of the linear JPA gain.

Under these assumptions, there is a linear relationship between the gain of the JPA and R_{PSD}. This ratio is measured for several gain values [Fig. 10(b)] at frequency $\omega_p/2\pi = 6.913$ GHz. From the measured slope $[(1-\eta)(T_{\mathrm{JPA}}+T_{\mathrm{in}})/T_{\mathrm{HEMT}} \simeq 1/22.7]$, we can estimate the noise temperature of the JPA, at frequency ω_p. Indeed, the ratio $T_{\mathrm{HEMT}}/(1-\eta)$ is measured to be 8 ± 2 K in this setup [46]. This translates into $T_{\mathrm{JPA}} = 180 \pm 90$ mK, corresponding to a number of added photons 0.55 ± 0.25, while the quantum limit stands at 0.50 [47]. Moreover, this PSD ratio is comparable to what was reported by other groups [8]. In conclusion, we present evidence that the JPA reported in this work is near quantum limited, but the uncertainty of our measurement prevents us from claiming that it performs strictly at the quantum limit.

[1] J. Y. Mutus, T. C. White, R. Barends, Y. Chen, Z. Chen, B. Chiaro, A. Dunsworth, E. Jeffrey, J. Kelly, A. Megrant, C. Neill, P. J. J. O'Malley, P. Roushan, D. Sank, A. Vainsencher, J. Wenner, K. M. Sundqvist, A. N. Cleland, and J. M. Martinis, Strong environmental coupling in a Josephson parametric amplifier, Appl. Phys. Lett. **104**, 263513 (2014).

[2] T. Roy, S. Kundu, M. Chand, and A. M. Vadiraj, Broadband parametric amplification with impedance engineering: Beyond the gain-bandwidth product, Appl. Phys. Lett. **107**, 262601 (2015).

[3] T. Yamamoto, K. Inomata, M. Watanabe, K. Matsuba, T. Miyazaki, W. D. Oliver, Y. Nakamura, and J. S. Tsai, Flux-driven Josephson parametric amplifier, Appl. Phys. Lett. **93**, 042510 (2008).

[4] N. Bergeal, F. Schackert, M. Metcalfe, R. Vijay, V. E. Manucharyan, L. Frunzio, D. E. Prober, R. J. Schoelkopf, S. M. Girvin, and M. H. Devoret, Phase-preserving amplification near the quantum limit with a Josephson ring modulator, Nature **465**, 64 (2010).

[5] N. Roch, E. Flurin, F. Nguyen, and P. Morfin, Widely Tunable, Nondegenerate Three-Wave Mixing Microwave Device Operating Near the Quantum Limit, Phys. Rev. Lett. **108**, 147701 (2012).

[6] J. Y. Mutus, T. C. White, E. Jeffrey, D. Sank, R. Barends, J. Bochmann, Y. Chen, Z. Chen, B. Chiaro, A. Dunsworth, J. Kelly, A. Megrant, C. Neill, P. J. J. O'Malley, P. Roushan, A. Vainsencher, J. Wenner, I. Siddiqi, R. Vijay, A. N. Cleland, and J. M. Martinis, Design and characterization of a lumped element single-ended superconducting microwave parametric amplifier with on-chip flux bias line, Appl. Phys. Lett. **103**, 122602 (2013).

[7] C. Eichler, Y. Salathe, J. Mlynek, S. Schmidt, and A. Wallraff, Quantum-Limited Amplification and Entanglement in Coupled Nonlinear Resonators, Phys. Rev. Lett. **113**, 110502 (2014).

[8] N. E. Frattini, U. Vool, S. Shankar, A. Narla, K. M. Sliwa, and M. H. Devoret, 3-Wave mixing Josephson dipole element, Appl. Phys. Lett. **110**, 222603 (2017).

[9] B. Abdo, K. Sliwa, L. Frunzio, and M. Devoret, Directional Amplification with a Josephson Circuit, Phys. Rev. X **3**, 031001 (2013).

[10] K. M. Sliwa, M. Hatridge, A. Narla, S. Shankar, L. Frunzio, R. J. Schoelkopf, and M. H. Devoret, Reconfigurable Josephson Circulator/Directional Amplifier, Phys. Rev. X **5**, 041020 (2015).

[11] F. Lecocq, L. Ranzani, G. A. Peterson, K. Cicak, R. W. Simmonds, J. D. Teufel, and J. Aumentado, Nonreciprocal Microwave Signal Processing with a Field-Programmable Josephson Amplifier, Phys. Rev. Appl. **7**, 024028 (2017).

[12] B. Abdo, F. Schackert, M. Hatridge, C. Rigetti, and M. Devoret, Josephson amplifier for qubit readout, Appl. Phys. Lett. **99**, 162506 (2011).

[13] C. Eichler, Ph.D. thesis, School ETH Zurich, 2013.

[14] C. Eichler and A. Wallraff, Controlling the dynamic range of a Josephson parametric amplifier, EPJ Quantum Technol. **1**, 2 (2014).

[15] X. Zhou, V. Schmitt, P. Bertet, D. Vion, W. Wustmann, V. Shumeiko, and D. Esteve, High-gain weakly nonlinear flux-modulated Josephson parametric amplifier using a SQUID array, Phys. Rev. B **89**, 214517 (2014).

[16] A. W. Eddins, Ph.D. thesis, School University of California, Berkeley, 2017.

[17] G. Liu, T. C. Chien, X. Cao, O. Lanes, E. Alpern, D. Pekker, and M. Hatridge, Josephson parametric converter saturation and higher order effects, Appl. Phys. Lett. **111**, 202603 (2017).

[18] N. E. Frattini, V. V. Sivak, A. Lingenfelter, S. Shankar, and M. H. Devoret, Optimizing the Nonlinearity and Dissipation of a SNAIL Parametric Amplifier for Dynamic Range, Phys. Rev. Appl. **10**, 054020 (2018).

[19] B. Yurke and E. Buks, Performance of cavity-parametric amplifiers, employing Keff nonlinearites, in the presence of two-photon loss, J. Lightwave Technol. **24**, 5054 (2006).

[20] B. A. Kochetov and A. Fedorov, Higher-order nonlinear effects in a Josephson parametric amplifier, Phys. Rev. B **92**, 224304 (2015).

[21] S. Boutin, D. M. Toyli, A. V. Venkatramani, A. W. Eddins, I. Siddiqi, and A. Blais, Effect of Higher-Order Nonlinearities on Amplification and Squeezing in Josephson Parametric Amplifiers, Phys. Rev. Appl. **8**, 054030 (2017).

[22] B. Yurke, M. L. Roukes, R. Movshovich, and A. N. Pargellis, A low-noise series-array Josephson junction parametric amplifier, Appl. Phys. Lett. **69**, 3078 (1996).

[23] M. A. Castellanos-Beltran, K. D. Irwin, G. C. Hilton, L. R. Vale, and K. W. Lehnert, Amplification and squeezing of quantum noise with a tunable Josephson metamaterial, Nat. Phys. **4**, 928 (2008).

[24] P. Lähteenmäki, G. S. Paraoanu, J. Hassel, and P. J. Hakonen, Dynamical Casimir effect in a Josephson metamaterial, Proc. Natl. Acad. Sci. **110**, 4234 (2013).

[25] V. Vesterinen, O.-P. Saira, I. Räisänen, M. Möttönen, L. Grönberg, J. Pekola, and J. Hassel, Lumped-element Josephson parametric amplifier at 650 MHz for nanocalorimeter readout, Supercond. Sci. Technol. **30**, 085001 (2017).

[26] Y. Krupko, V. D. Nguyen, T. Weissl, E. Dumur, J. Puertas, R. Dassonneville, C. Naud, F. W. J. Hekking, D. M. Basko, O. Buisson, N. Roch, and W. Hasch-Guichard, Kerr nonlinearity in a superconducting Josephson metamaterial, Phys. Rev. B **98**, 094516 (2018).

[27] R. Vijay, M. Devoret, and I. Siddiqi, Invited review article: The Josephson bifurcation amplifier, Rev. Sci. Instrum. **80**, 111101 (2009).

[28] E. A. Tholen, A. Ergul, E. M. Doherty, F. M. Weber, F. Gregis, and D. B. Haviland, Nonlinearities and parametric amplification in superconducting coplanar waveguide resonators, Appl. Phys. Lett. **90**, 253509 (2007).

[29] C. C. Chin, D. E. Oates, G. Dresselhaus, and M. S. Dresselhaus, Nonlinear electrodynamics of superconducting NbN and Nb thin films at microwave frequencies, Phys. Rev. B **45**, 4788 (1992).

[30] N. Maleeva, L. Grünhaupt, T. Klein, F. Levy-Bertrand, O. Dupré, M. Calvo, F. Valenti, P. Winkel, F. Friedrich, W. Wernsdorfer, A. V. Ustinov, H. Rotzinger, A. Monfardini, M. V. Fistul, and I. M. Pop, Circuit quantum electrodynamics of granular aluminum resonators, Nat. Commun. **9**, 3889 (2018).

[31] J. Bourassa, F. Beaudoin, J. M. Gambetta, and A. Blais, Josephson-junction-embedded transmission-line resonators: From Kerr medium to in-line transmon, Phys. Rev. A **86**, 013814 (2012).

[32] C. Eichler, C. Lang, J. M. Fink, J. Govenius, S. Filipp, and A. Wallraff, Observation of Entanglement between Itinerant Microwave Photons and a Superconducting Qubit, Phys. Rev. Lett. **109**, 240501 (2012).

[33] S. E. Nigg, H. Paik, B. Vlastakis, G. Kirchmair, and S. Shankar, Black-box superconducting circuit quantization, Phys. Rev. **108**, 260 (2012).

[34] T. Weissl, B. Küng, E. Dumur, A. K. Feofanov, I. Matei, C. Naud, O. Buisson, F. W. J. Hekking, and W. Guichard, Kerr coefficients of plasma resonances in Josephson junction chains, Phys. Rev. B **92**, 104508 (2015).

[35] T. Roy, M. Chand, A. Bhattacharjee, S. Hazra, S. Kundu, K. Damle, and R. Vijay, Multimode superconducting circuits for realizing strongly coupled multiqubit processor units, Phys. Rev. A **98**, 052318 (2018).

[36] D. M. Pozar, *Microwave Engineering* (John Wileyand Sons, Inc., Hoboken, NJ, 2005), 3rd ed.

[37] F. Lecocq, I. M. Pop, Z. Peng, I. Matei, T. Crozes, T. Fournier, C. Naud, W. Guichard, and O. Buisson, Junction fabrication by shadow evaporation without a suspended bridge, Nanotechnology **22**, 315302 (2011).

[38] A. Fay, Ph.D. thesis, School Université Joseph-Fourier - Grenoble I, 2008.

[39] N. Masluk, I. Pop, A. Kamal, Z. Minev, and M. Devoret, Microwave Characterization of Josephson Junction Arrays: Implementing a Low Loss Superinductance, Phys. Rev. Lett. **109**, 137002 (2012).

[40] M. Hatridge, R. Vijay, D. H. Slichter, J. Clarke, and I. Siddiqi, Dispersive magnetometry with a quantum limited SQUID parametric amplifier, Phys. Rev. B **83**, 134501 (2011).

[41] C. Macklin, K. O'Brien, D. Hover, M. Schwartz, V. Bolkhovsky, X. Zhang, W. Oliver, and I. Siddiqi, A near–quantum-limited Josephson traveling-wave parametric amplifier, Science **350**, 307 (2015).

[42] T. White, J. Mutus, I.-C. Hoi, R. Barends, B. Campbell, Y. Chen, Z. Chen, B. Chiaro, A. Dunsworth, and E. Jeffrey *et al.*, Traveling wave parametric amplifier with Josephson junctions using minimal resonator phase matching, Appl. Phys. Lett. **106**, 242601 (2015).

[43] M. Simoen, C. W. S. Chang, P. Krantz, J. Bylander, W. Wustmann, V. Shumeiko, P. Delsing, and C. M. Wilson, Characterization of a multimode coplanar waveguide parametric amplifier, J. Appl. Phys. **118**, 154501 (2015).

[44] J. Koch, T. M. Yu, J. Gambetta, A. A. Houck, D. I. Schuster, J. Majer, A. Blais, M. H. Devoret, S. M. Girvin, and R. J. Schoelkopf, Charge-insensitive qubit design derived from the Cooper pair box, Phys. Rev. A **76**, 042319 (2007).

[45] Z. R. Lin, K. Inomata, W. D. Oliver, K. Koshino, Y. Nakamura, J. S. Tsai, and T. Yamamoto, Single-shot readout of a superconducting flux qubit with a flux-driven Josephson parametric amplifier, Appl. Phys. Lett. **103**, 132602 (2013).

[46] E. Dumur, Ph.D. thesis, School University Grenoble Alpes, 2015.

[47] C. M. Caves, Quantum limits on noise in linear amplifiers, Phys. Rev. D **26**, 1817 (1982).